Article

Highly Accessible Co−N$_x$ Active Sites-Doped Carbon Framework with Uniformly Dispersed Cobalt Nanoparticles for the Oxygen Reduction Reaction in Alkaline and Neutral Electrolytes

Peipei Liu,[#] Meiling Fan,[#] Yapeng Cheng,* Hongfei Pan, Jin Liu,* and Haining Zhang

Cite This: ACS Omega 2024, 9, 1001−1010

Read Online

ACCESS | Metrics & More | Article Recommendations | SI Supporting Information

ABSTRACT: Porous carbon materials with nitrogen-coordinated transition metal active sites have been widely regarded as appealing alternatives to replace noble metal catalysts in oxygen-based electrochemical reaction activities. However, improving the electrocatalytic activity of transition-metal-based catalysts remains a challenge for widespread application in renewable devices. Herein, we use a simple one-step pyrolysis method to construct a Co nanoparticles/Co−N$_x$-decorated carbon framework catalyst with a near-total external surface structure and uniform dispersion nanoparticles, which displays promising catalytic activity and superior stability for oxygen reduction reactions in both alkaline and neutral electrolytes, as evidenced by the positive shift of half-wave potential by 44 and 11 mV compared to 20% Pt/C. Excellent electrochemical performance originates from highly accessible Co nanoparticles/Co−N$_x$ active sites at the external surface structure (this is, exposing active sites). The thus-assembled liquid zinc−air battery using the synthesized electrocatalyst as the cathode material delivers a maximum power density of 178 mW cm^{-2} with an open circuit potential of 1.48 V and long-term discharge stability over 150 h.
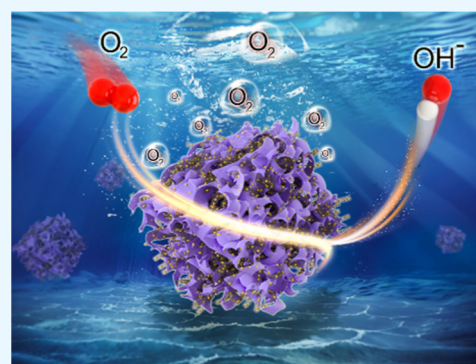
1. INTRODUCTION

With the increased concerns about the energy crisis, rapid climate change, and environmental pollution caused by the overuse of fossil fuels, the development of new sustainable energy sources is of great importance for safe future energy generation.[1,2] Fuel cells and metal−air batteries have been considered promising viable alternatives to the depleting fossil energy resources due to their high theoretical energy density, safety, and eco-friendly nature.[3−5] Fuel cells and metal−air batteries are oxygen-involved electrochemical energy conversion devices in which the electrocatalytic oxygen reduction reaction (ORR) is the key half-reaction determining the performance of devices. Due to the sluggish kinetics of the ORR, Pt-based materials are still considered the ideal and practical electrocatalysts.[6,7] However, the limited reserves, high cost, and poor stability of Pt-based catalysts hinder their widespread applications. Transition metal-based electrocatalysts, including metallic nanoparticles, metallic clusters, and metallic single atoms, have been extensively studied. This is because the lone pair electrons of oxygen molecules can easily coordinate with the vacant 3d orbitals of transition metals, a significant factor in the process of oxygen adsorption.[8−10]

In recent years, carbon-supported transition metal−nitrogen/carbon complexes (M−N/C, M = Fe, or Co) catalysts have received extensive attention due to their superior activity in oxygen electrocatalysis.[11−13] For M−N/C electrocatalysts, the transition metal-coordinated nitrogen (M−N$_x$) are widely regarded as the active center of the oxygen reduction reaction.[14,15] According to Sabatier's principle, the high ORR activity of the M−N$_x$ active site may be related to the moderate adsorption strength between the ORR intermediate and the active site.[16] The catalytic reaction rate of the catalyst is directly related to the number of effectively participated M−N$_x$ active sites in the skeleton, and considering that the M−N$_x$ active sites hardly participate in the reaction process, increasing accessible active sites is an effective way to improve mass transport and increase catalytic activities. In order to expose more active sites, increasing the high external structure of the catalyst is an ideal way, as active sites near the external surface area are preferred for catalyzing electrochemical activities.[17] According to Feng et al., large-size nanoparticles should be avoided to maximize the number of active sites; thus, fabricating uniformly dispersed nanoparticles is required for further design.[18]

Herein, highly accessible Co−N$_x$ active sites-doped carbon frameworks with uniformly dispersed cobalt nanoparticles are prepared through one-step pyrolysis of cobalt salts-embedded,

cobalt salts-dispersed poly glucose intercalated g-C_3N_4 nanosheets. First, the flower-shaped supermolecule melamine cyanurate (MCA) is synthesized as the nitrogen source and skeleton for anchoring metallic ions, which is significant for dispersing ZIF-67 frameworks. In addition, low-cost and environmentally friendly biomass glucose is used as the carbon source. During carbonization, the composite multidimensional structures could effectively avoid the aggregation of metallic nanoparticles effectively and the introduction of glucose through a hydrogen bond contributes to the increased external surface area derived from sugar burst phenomena. The dispersed nanoparticles and large external specific surface area increase the utilization of Co−N_x active sites. The thus-assembled liquid zinc−air batteries assembled using the synthesized material as a cathode catalyst show high open circuit voltage, large peak power density, and great rate capability.

2. EXPERIMENTAL SECTION

2.1. Reagents and Materials. Cobalt(II) acetate tetrahydrate [Co(OAc)$_2$·4H$_2$O] and dimethyl sulfoxide (DMSO) were received from Sinoreagent (Shanghai, China). Melamine, 2-methylimidazole, cyanuric acid, and glucose were all obtained from Aladdin (Shanghai, China). All reagents were used directly without further purification.

2.2. Synthesis of MCA-ZIF-67-C. 1 g portion of melamine and 0.05 g of Co(OAc)$_2$·4H$_2$O were added to 40 mL of DMSO under stirring for 30 min to form uniform purple solution A. Meanwhile, 1 g of cyanuric acid, 0.13 g of 2-methylimidazole, and 8 g of glucose were dissolved in 20 mL of DMSO to form transparent solution B. Solution A was poured slowly into solution B, and the clear purple solution transferred into bluish violet emulsion quickly. After keeping stirring for another 2.5 h, the precipitate was centrifuged and washed with ethanol until the supernatant became colorless. MCA-ZIF-67-C was finally obtained after the precipitate was dried in the oven for 12 h at 60 °C.

2.3. Synthesis of MCA-ZIF-67. MCA-ZIF-67 was synthesized with a similar process to MCA-ZIF-67-C, except without the addition of glucose to solution B.

2.4. Synthesis of MCA-Co. MCA-Co was received with a similar process to MCA-ZIF-67-C, except without the addition of melamine in solution A, 2-methylimidazole, and cyanuric acid in solution B.

2.5. Synthesis of ZIF-67. ZIF-67 was obtained with a similar process to MCA-ZIF-67, except without the addition of melamine in solution A and cyanuric acid in solution B, respectively.

2.6. Synthesis of MCA. MCA was received with a similar process to that of MCA-ZIF-67, except without the addition of Co(OAc)$_2$·4H$_2$O in solution A and 2-methylimidazole in solution B, respectively.

2.7. Synthesis of Co-N/C-800@MCA-ZIF-67-C. The prepared MCA-ZIF-67-C precursor was put in the tube furnace, filled with high-purity Ar. After 40 min, the precursor was pyrolyzed under 800 °C for 2 h with a ramp rate of 2 °C min^{-1}, and the tube was further filled with H$_2$/Ar (5 vol %) during carbonization. Co-N/C-800@MCA-ZIF-67-C was finally received after the tube furnace cooled to room temperature. In addition, Co-N/C-800@MCA-ZIF-67, Co-N/C-800@MCA-Co, and Co-N/C-800@ZIF-67 were obtained through pyrolyzing MCA-ZIF-67, MCA-Co, and ZIF-67 precursors under the same process. To explore the influence

of pyrolysis temperature on the catalytic performance, the MCA-ZIF-67-C precursor was also carbonized at 700 and 900 °C under the same ramp rate, and the as-received samples were labeled as Co-N/C-700@MCA-ZIF-67-C and Co-N/C-900@MCA-ZIF-67-C.

2.8. General Characterizations. X-ray diffraction (XRD) patterns were collected by a D8 Advance powder X-ray diffractometer (Bruker, Germany) with a scan rate of 5° min^{-1} in the 2θ range of 5−70° using u Kα radiation (λ = 1.5406 Å). Raman spectroscopy was performed on an InVia RENISHAW Raman microscope (RENISHAW, UK). Scanning electron microscopy (SEM) images were taken from a Zeiss Sigma300 scanning electron microscope operating at a 5 kV accelerating voltage. Nitrogen adsorption−desorption experiments were carried out at 77 K, and the Brunauer−Emmett−Teller (BET) method was applied to calculate the specific surface areas. A ESCALAB 250Xi XPS photoelectron spectrometer (Thermo, USA) was used for X-ray photoelectron spectroscopy (XPS) with Al Kα radiation. All the XPS data were fitted by the Thermo Avantage software (Thermo Scientific). Transmission electron microscopy (TEM) images were collected from a FEITecnai G2 F30 S microscope (FEI, America) operating at 200 kV.

2.9. Electrochemical Measurements. Electrochemical tests were performed on an electrochemical workstation CHI660E with a three-electrode system. Before electrochemical measurements, catalyst ink was prepared by dispersing 3 mg of sample in 1 mL of solvent containing 760 μL of isopropanol, 200 μL of deionized water, and 40 μL of Nafion (5 wt %) solution under ultrasonication for 30 min. During electrochemical tests, glass carbon electrodes (0.196 cm^2) coated with catalyst (0.18 mg cm^{-2}), Pt foil, and Ag/AgCl were used as the working electrode, counter electrode and reference electrode, respectively. Linear sweep voltammetry (LSV) measurements were performed in N$_2$/O$_2$-saturated 0.1 M KOH and 0.1 M Na$_2$SO$_4$ with scan rates at 5 mV s^{-1}.

2.10. Zn−Air Battery Measurement. The zinc−air battery was assembled using a polished zinc plate (0.5 mm) as the anode, carbon paper coated with a catalyst (1.0 mg cm^{-2}) as the air cathode, and 6 M KOH containing 0.2 M Zn(OAc)$_2$ aqueous solution as the electrolyte. The effective area of the air cathode was 1 cm^2, and all data were recorded on an electrochemical working station CHI760E. The polarization curve was received with a scan rate of 10 mV s^{-1}. The durability performance was characterized by discharging under 10 mA cm^{-2} for 150 h. For comparison, carbon paper-coated 20 wt % Pt/C with the same loading was used as the air cathode for the zinc−air battery test.

2.11. Flexible Solid-State Zinc−Air Battery Measurement. The flexible solid-state zinc−air battery was assembled using a polished zinc plate as the anode and carbon cloth coated with catalyst (1.0 mg cm^{-2}) as the air cathode. Glass fiber (1 cm^2) containing 6 M KOH and 0.2 M Zn(OAc)$_2$ aqueous solution served as the solid-state electrolyte. The effective area of the air cathode was 1 cm^2, and all data were recorded on an electrochemical working station CHI760E. The polarization curve was received with a scan rate of 10 mV s^{-1}. The durability performance was characterized through discharging at 1 mA cm^{-2} under flat, 60, and 180° for 30 min, respectively. For comparison, carbon cloth-coated 20 wt % Pt/C with the same loading served as the air cathode for the flexible solid-state zinc−air battery test.
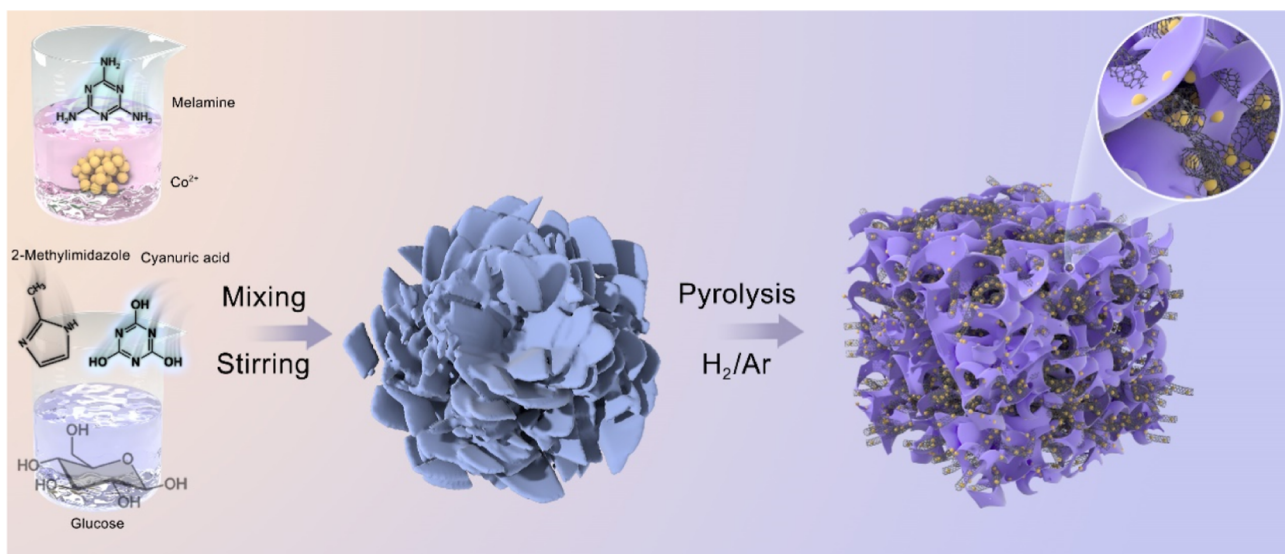
Figure 1. Schematic illustration of the synthesis of Co-N/C-800@MCA-ZIF-67-C.

3. RESULTS AND DISCUSSION

The synthetic process of the Co-N/C-800@MCA-ZIF-67-C catalyst is schematically illustrated in Figure 1. Briefly, the ZIF-67-decorated flower-shaped MCA-ZIF-67-C was self-assembled at room temperature through the induction of DMSO. Meanwhile, glucose was introduced into the frameworks through the formation of hydrogen bonds between glucose and melamine. During carbonization, Co^{2+} was reduced to Co nanoparticles with the disintegration of ZIF-67 frameworks, and bamboo-shaped carbon nanotubes were formed under simultaneous catalysis of Co nanoparticles simultaneously.

Accordingly, at 550 °C, the layered flower-shaped MCA generates a carbon intercalation layer, g-C_3N_4 in the presence of glucose, which is gradually exfoliated into carbon nanosheets during subsequent pyrolysis to form a structure in which the cobalt nanoparticles are highly dispersed on the carbon skeleton.

To investigate the morphology and microstructure of Co-N/C-800@MCA-ZIF-67-C, SEM images were first taken. As shown in Figure 2a, carbon nanotubes and carbon nanosheets coexist in Co-N/C-800@MCA-ZIF-67-C, and the bamboolike carbon nanotubes and nanosheets are interspersed with each other, which greatly increases the specific surface area of the material. Similarly, a composite of carbon nanosheets and carbon nanotubes was also observed in Figure S1a,b for Co-N/C-700@MCA-ZIF-67-C and Co-N/C-900@MCA-ZIF-67-C. Moreover, the quantity and diameter of carbon nanotubes increase as the pyrolysis temperature increases to 900 °C. In addition, abundant pores were formed during the formation of carbon nanotubes. For samples derived from MCA-ZIF-67, as displayed in Figure S1c, no obvious carbon nanosheets could be observed, and the length−diameter of Co-N/C-800@MCA-ZIF-67 was much larger than that of samples carbonized from MCA-ZIF-67-C.

TEM and HR-TEM techniques were applied to characterize the microscopic and crystalline structures of samples. As displayed in Figures 2b and S2, metallic nanoparticles were clearly observed in all samples. For Co-N/C-800@MCA-ZIF-67-C, metallic nanoparticles with an average size of 10 nm were uniformly distributed in the carbon frameworks. With the
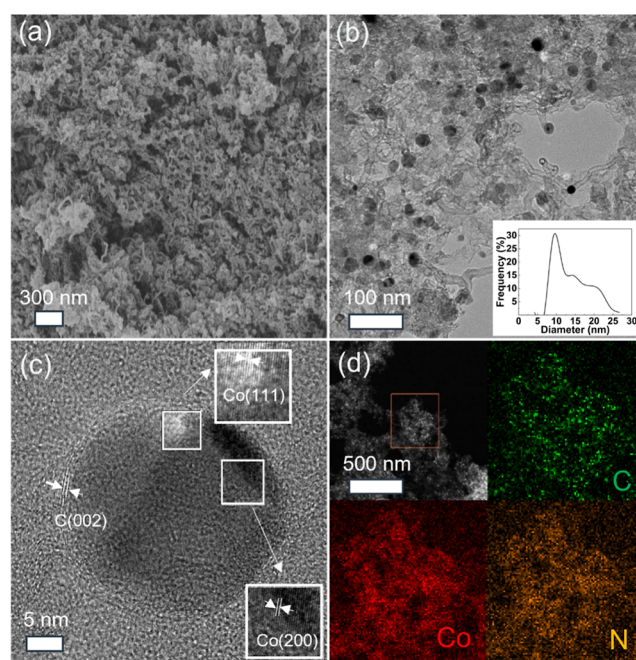

Figure 2. SEM image (a), TEM image (b), HR-TEM image (c), HAADF-TEM image, and elemental distributions of Co, N, and C (d) of Co-N/C-800@MCA-ZIF-67-C.

increase in the pyrolysis temperature, the particles became larger, and the morphology of the nanoparticles became irregular. As revealed in Figure S3, the Co nanoparticles in Co-N/C-800@MCA-ZIF-67-C were more uniformly distributed, with an average size of 10 nm, compared to the morphology of Co-N/C-800@MCA-ZIF-67, indicating that the introduction of glucose into the precursor had a significant effect on the dispersion of metal nanoparticles. Highly dispersed metal nanoparticles are conducive to exposing more active sites and improving ORR performance.[19] To investigate the crystalline structure of metallic nanoparticles, the HR-TEM image of Co-N/C-800@MCA-ZIF-67-C is displayed in Figure 2c. Two obvious lattice fringes of the metal phase corresponding to the Co(111) plane and Co(200) plane of metallic Co nano-
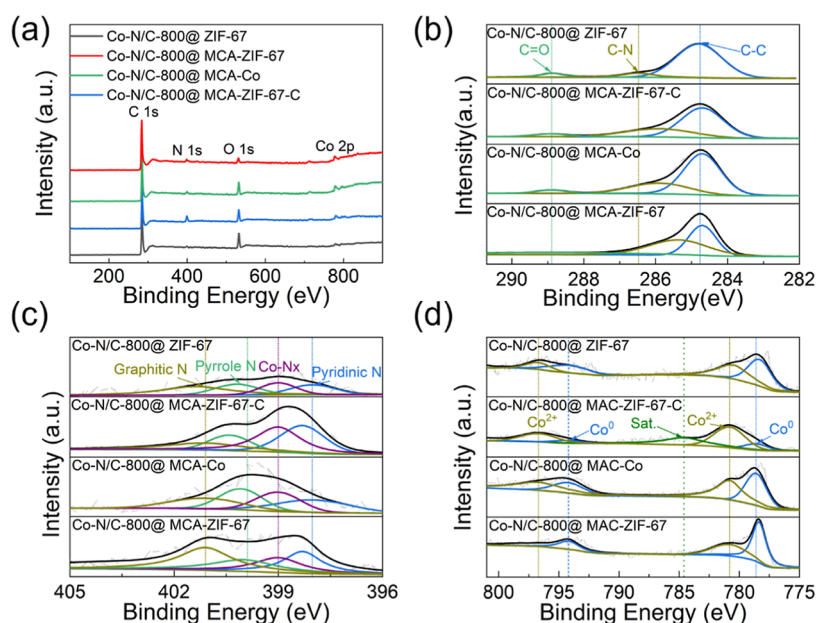
Figure 3. XPS full surveys (a), high-resolution XPS spectra, and deconvolution results of C 1s (b), N 1s (c), and Co 2p (d) for samples indicated in the figure.

particles were observed, suggesting successful doping of Co elements into carbon framework.[20] Thin carbon layers with the C(002) plane of graphitic carbon have been observed around the Co nanoparticles, which can reduce the corrosion of metal nanoparticles and therefore enhance the stability of the catalyst.[21] The HAADF-TEM and elemental distribution images of Co-N/C-800@MCA-ZIF-67-C are displayed in Figure 2d. It is shown that Co, N, and C elements were uniformly dispersed in the sample, and N doping and Co nanoparticles could act as active sites to improve the ORR performance.[22,23]

The XPS technique was applied to test the near-surface element composition and chemical state of samples. C, N, O, and Co elements were clearly observed in the XPS surveys (Figure 3a). The accordingly calculated element content is listed in Table S1, and Co-N/C-800@MCA-ZIF-67-C has the highest nitrogen content (13.23 at. %). The high-resolution C 1s spectra are shown in Figure 3b, which can be deconvoluted into three peaks at 284.7, 286.5, and 288.9 eV, corresponding to C−C, C−N, and C=O bonds, respectively.[24−26] The high-resolution N 1s spectra (Figure 3c) can be deconvoluted into four peaks located at 398.3, 399, 400, and 401.1 eV, corresponding to pyridinic N, Co−N$_x$, pyrrolic N, and graphitic N, respectively.[27,28] This proves the coordination of Co and N in the carbon framework. The Co−N$_x$ active sites help tune the charge distribution and electronic properties of the electrocatalysts, promote the adsorption of reaction intermediates, and further enhance the corresponding reaction activities.[29−32] The nitrogen content for Co-N/C-800@MCA-ZIF-67-C is 13.23%, as listed in Table S1. Both pyridine N and graphite N coordinate with Co to form Co−N$_x$ molecules, and the nitrogen atoms are stabilized in the carbon matrix through the formation of Co−N bonds, which are progressively lost once the cobalt nanoparticles are aggregated because the remaining N−C bonds cannot effectively bind the carbon atoms without the presence of Co−N bonds.[33,34] Considering that the valence state of the Co element is significant for the electrochemical performance of the sample, the peak

deconvolution of Co 2p for all samples is displayed in Figure 3d. Two main peaks at 780.8 and 796.7 eV could be attributed to Co^{2+}, while peaks centered at 778.6 and 794.2 eV suggest the presence of Co^0.[35−38] There were also only Co^{2+} and Co^0 valence states for samples carbonized under diverse temperatures, as shown in Figure S4d. The accurate Co contents of samples were obtained through the ICP test. As shown in Figure S5, Co-N/C-800@MCA-ZIF-67-C had a Co content of 15.3%, almost one-half of Co-N/C-800@MCA-ZIF-67. The higher Co content and lower nitrogen content in Co-N/C-800@MCA-ZIF-67 may suggest more serious agglomeration of metallic particles, as indicated by TEM results, leading to the inefficient utilization of active sites.

To further verify the crystal structures of the samples, XRD patterns were recorded. As shown in Figure 4a, three main diffraction peaks were observed at 44.2, 51.5, and 75.9°,
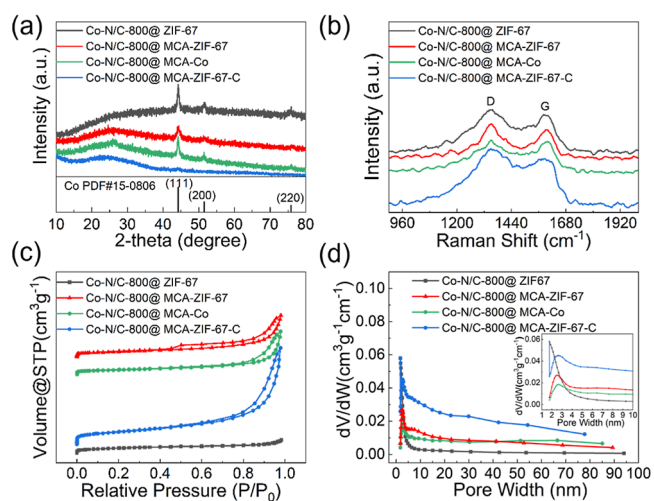

Figure 4. XRD patterns (a), Raman spectra (b), N$_2$ adsorption−desorption isotherms (c), and pore size distribution diagram (d) of samples.
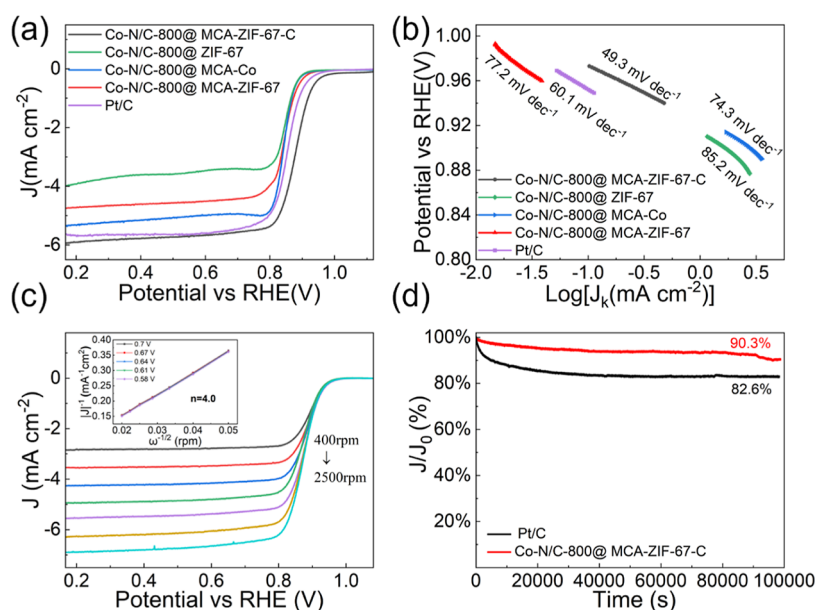
Figure 5. (a) LSV curves of samples at 1600 rpm in O_2-saturated 0.1 M KOH, (b) Tafel slopes calculated from LSV curves, (c) LSV curves of Co-N/C-800@MCA-ZIF-67-C at different rotation rates, and (d) durability test.

attributed to the (111), (200), and (220) planes of metallic Co (JCPDS no. 89-4307),[39] indicating that Co elements were doped into carbon frameworks in the form of metallic Co. In addition, a peak appeared at 23.8° for all samples corresponded to the (002) crystalline surface of graphitic carbon,[40] consistent with the HR-TEM result. It was observed that the peak intensity at 44.2° became stronger as the pyrolysis temperature increased to 900 °C, as listed in Figure S6a, indicating a higher crystallinity of Co-N/C-900@MCA-ZIF-67-C.[41]

Considering the significant impact of the graphitization degree on the catalytic performance of samples, Raman spectroscopy was performed to characterize the degree of graphitization. As shown in Figure 4b, two obvious peaks observed at 1350 and 1580 cm^{-1} corresponded to the D band and G band of the carbon atoms.[42,43] The D band is usually associated with the disorder of carbon material, and the intensity ratio of I_D/I_G reflects the degree of defects in the carbonized material.[44,45] The calculated I_D/I_G value of Co-N/C-800@MCA-ZIF-67-C, as shown in Table S1, is 1.48, larger than those of Co-N/C-800@MCA-Co (1.07) and Co-N/C-800@MCA-ZIF-67 (1.26), indicating a higher degree of defects in Co-N/C-800@MCA-ZIF-67-C, which is favorable for improved ORR performance.[46] In addition, the lowest I_D/I_G value of Co-N/C-900@MCA-ZIF-67-C suggests that increasing the carbonization temperature could enhance the graphitization degree of samples.[47]

N_2 adsorption−desorption measurement was applied to characterize the porous structures and BET surface area of samples, as displayed in Figure 4c,d. Obvious hysteresis loops were observed for Co-N/C-800@MCA-ZIF-67-C, Co-N/C-800@MCA-Co, and Co-N/C-800@MCA-ZIF-67, indicating the existence of abundant porous structures in those samples.[48] The BJH pore size distribution curves suggest that the pore size of samples mainly concentrates at around 2.66 nm, which is beneficial for O_2 adsorption, as reported in the literature.[49] The calculated specific surface areas of the samples are listed in Table S2. Usually, the effective active sites in the catalyst are prior to existing at the external surface area of the catalytic

activities, as they can be directly exposed outside to quickly absorb those small reacting molecules, while the buried active sites hardly stay active. Surprisingly, the external surface area of Co-N/C-800@MCA-ZIF-67-C (462.71 m^2 g^{-1}) is much larger than that of Co-N/C-800@MCA-ZIF-67 (186.33 m^2 g^{-1}), which benefits exposing accessible active sites and thus enhancing mass transport.[50−53] The improved specific surface area derives from the contributions of ZIF-67 and glucose frameworks in the precursor. The introduction of glucose could prevent the agglomeration of the ZIF-67 skeletons, which is significant for the formation of porous structures. In addition, the decomposition of MCA is helpful for pore generation.

The electrocatalytic performance of samples was characterized using a three-electrode system, using Pt foil as the counter electrode and Ag/AgCl (saturated KCl) as the reference electrode, respectively. LSV curves were recorded at 10 mV s^{-1} in O_2-saturated 0.1 M KOH. As displayed in Figure 5a, Co-N/C-800@MCA-ZIF-67-C had the highest half-wave potential (0.88 V), almost 30 mV higher than that of the Pt/C catalyst. While Co-N/C-800@MCA-metal and Co-N/C-800@MCA-ZIF-67 exhibited similar half-wave potential at about 0.84 V. Tafel slopes calculated from LSV curves are shown in Figure 5b. The Tafel slope of Co-N/C-800@MCA-ZIF-67-C was 49.3 mV dec^{-1}, much lower than those of other samples, indicating the fastest kinetic process of the ORR among all of the tested samples. The LSV curves of samples pyrolyzed at different temperatures are displayed in Figure S7a, and the derived Tafel plots are shown in Figure S7b. The sample at 800 °C has the smallest Tafel slope, indicating that the sample after being carbonized at 800 °C has better electrochemical properties. The excellent oxygen reduction properties of Co-N/C-800@MCA-ZIF-67-C might be attributed to the uniformly dispersed Co nanoparticles with smaller particle size induced by the sugar burst of glucose, large external specific surface area, abundant porous structures derived from the decomposition of g-C_3N_4, and ZIF-67 framework and the existence of Co−N_x active sites.
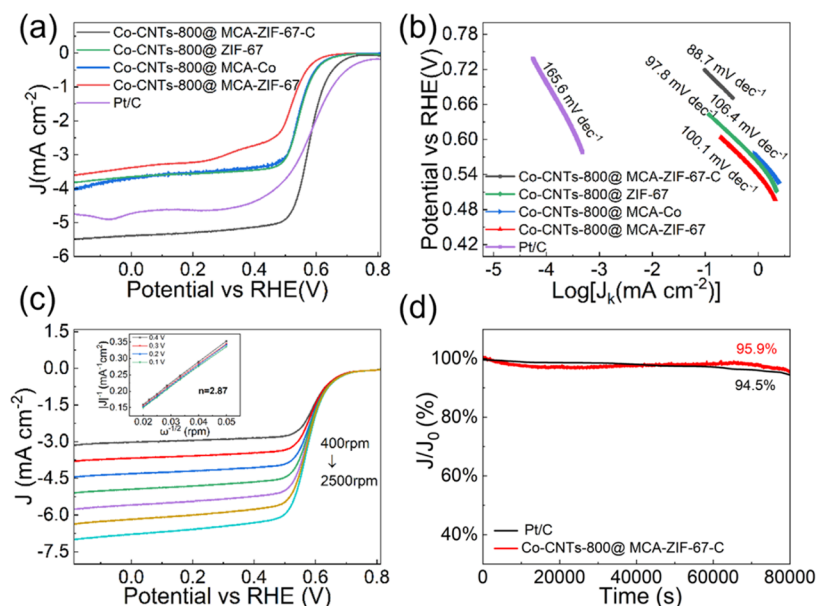
Figure 6. (a) LSV curves of samples at 1600 rpm in O_2-saturated 0.1 M Na_2SO_4, (b) Tafel slopes calculated from LSV curves, (c) LSV curves of Co-N/C-800@MCA-ZIF-67-C at different rotation rates, and (d) durability test.
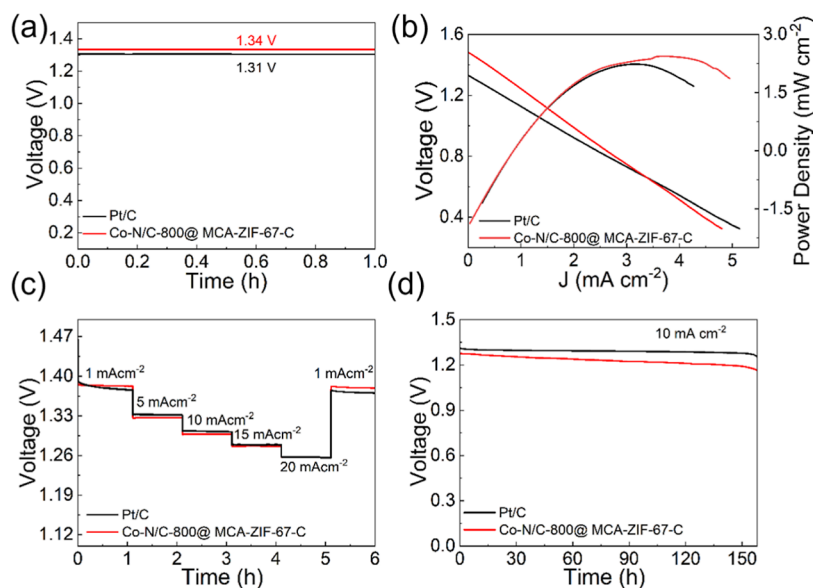

Figure 7. (a) Open-circuit voltages, (b) polarization curves of 10 mA cm^{-2}, (c) discharge curves under 1, 5, 10, 15, and 20 mA cm^{-2}, and (d) long-time discharge curve of zinc−air batteries using Co-N/C-800@MCA-ZIF-67-C and Pt/C as cathode catalysts.

To further understand the kinetics of the electrocatalytic process, LSV curves under diverse rotation rates for all samples are recorded in Figures 5c and S8. It was calculated from Koutecky−Levich equations that the electron transfer number (n) of Co-N/C-800@MCA-ZIF-67-C was about 4 (Figure 5d), indicating a four-electron transfer process of the ORR. Due to the crucial role of electrochemical active area on the performance of catalysts, CV curves of samples at different scan rates are listed in Figure S9. C_{dl} values calculated from the CV curves of Co-N/C-800@MCA-ZIF-67-C, Co-N/C-800@MCA-ZIF-67, Co-N/C@MCA-Co, and Co-N/C-800@ZIF-67 were 11.88, 3.67, 5.43, and 4.24 mF cm^{-2}, respectively. Similarly, the C_{dl} value of Co-N/C-800@MCA-ZIF-67-C was much higher than that of samples carbonized at 700 °C (5.27 mF cm^{-2}) and 900 °C (2.95 mF cm^{-2}), as shown in Figure

S10. A higher C_{dl} combined with the porous structure facilitated the permeability of the electrolyte solution and thus improved the utilization of available active sites.[54−56]

Stability is a crucial indicator to evaluate the catalytic performance of samples for practical applications; long-term durability and methanol tolerance tests of Co-N/C-800@ MCA-ZIF-67-C and commercial Pt/C catalysts were performed using an $i−t$ chronoamperometry at 0.47 V (vs RHE) for 98,000 s, as displayed in Figure 5d. The current density of Co-N/C-800@MCA-ZIF-67-C was 9.7% loss of the original current density after 98,000 s, while the current density of the commercial Pt/C catalyst was almost twice that of the target catalyst, indicating the superior endurance of Co-N/C-800@ MCA-ZIF-67-C. Moreover, Co-N/C-800@MCA-ZIF-67-C behaved better with methanol tolerance than Pt/C, and the

current density of the target catalyst hardly changed before and after adding methanol, as shown in Figure S11.

To further broaden the application of the catalysts, electrochemical measurements were performed in 0.1 M Na_2SO_4. As indicated by Figure 6a, the half-wave potential of both Co-N/C-800@MCA-ZIF-67-C and Pt/C was about 0.59 V. However, the limited current density of the target catalyst was 1 mA cm^{-2} higher than that of Pt/C. Besides, the Tafel slop of Co-N/C-800@MCA-ZIF-67-C is much lower than that of Pt/C shown in Figure 6b, suggesting different rate-determining steps of ORR in neutral electrolyte for the tested two catalysts.[57−59] For samples carbonized under different temperatures, Co-N/C-800@MCA-ZIF-67-C also exhibits the highest half-wave potential and lowest Tafel slope, as shown in Figure S12.

Different from the catalytic mechanism in 0.1 M KOH, the ORR in 0.1 M Na_2SO_4 is mainly a two-electrons path with an electron transfer number of about 2, as shown in Figures 6c and S13. Similar to the stability of samples in alkaline electrolytes, the current density of Co-N/C-800@MCA-ZIF-67-C only drops 4% after 80,000 s, as indicated by Figure 6d. In addition, the C_{dl} values for all samples in 0.1 M Na_2SO_4 follow a similar trend with those in 0.1 M KOH, as shown in Figures S14 and S15. However, the C_{dl} value of Co-N/C-800@MCA-ZIF-67-C is 7.39 mF cm^{-2}, much lower than that in 0.1 M KOH, indicating a smaller, more efficient electrochemical active surface.

3.1. Liquid Zinc−Air Battery Performance. Since the synthesized Co-N/C-800@MCA-ZIF-67-C exhibited a promising electrocatalytic activity for ORR, it was thus applied in a zinc−air battery using the catalyst-coated carbon paper as the cathode and the Zn plate as the anode. The open-circuit voltage of the Co-N/C-800@MCA-ZIF-67-C-based battery is 1.34 V, higher than that of the Pt/C-based battery (1.31 V) (Figure 7a). Besides, polarization curves were recorded to evaluate the battery performance. As shown in Figure 7b, the maximum power density calculated from polarization curves of the Co-N/C-800@MCA-ZIF-67-C-based battery was 178 mW cm^{-2}, almost 1.2 times higher than that of the Pt/C-based battery. Discharge curves at 1, 5, 10, 15, and 20 mA cm^{-2} in Figure 7c revealed that Co-N/C-800@MCA-ZIF-67-C exhibited considerable stability of discharge. The long-time discharge curves at 10 mA cm^{-2} of two zinc−air batteries are shown in Figure 7d. It can be seen that the Co-N/C-800@MCA-ZIF-67-C-based battery still maintains a voltage of about 1.2 V after 150 h.

A flexible solid Zn−air battery was also assembled, comprising a carbon cloth loaded with Co-N/C-800@MCA-ZIF-67-C (1 mg cm^{-2}) (acting as the air electrode), glass fiber with KOH (acting as the separator), and zinc foil (acting as the anode). As shown in Figure 8a, the open circuit voltage of the Co-N/C-800@MCA-ZIF-67-C-based solid-state zinc−air batteries is 1.52 V under flat conditions, higher than that of batteries under bending states. Moreover, the galvanostatic discharge curves of the Co-N/C-800@MCA-ZIF-67-C-based solid-state flexible zinc−air battery are presented in Figure 8b. It can be seen that the discharge voltage at 1 mA cm^{-2} remains stable at 0.9 V under flat conditions, higher than that of Pt/C (0.87 V).

4. CONCLUSIONS

In summary, a highly accessible Co−N$_x$ active sites-doped carbon framework with uniformly dispersed cobalt nano-
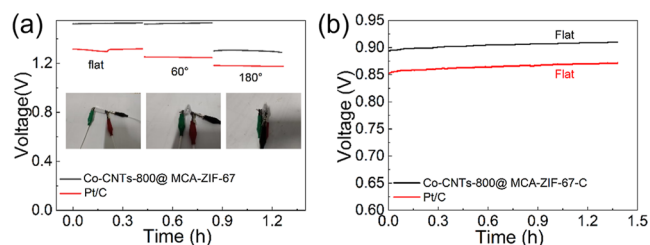

Figure 8. (a) Open-circuit voltage curves under flat, 60, and 180° conditions of the solid-state zinc−air batteries. (b) Discharge curves under flat and 180° conditions at 1 mA cm^{-2} of the Co-N/C-800@ MCA-ZIF-67-C-based solid-state zinc−air batteries.

particles is successfully synthesized through direct carbonization of a ZIF-67-decorated melamine cyanurate−glucose composite prepared by a solvent-induced method and the hydrogen-bonding effect. The high external surface area of Co-N/C-800@MCA-ZIF-67-C facilitates the exposure of more accessible active sites, resulting in excellent and preferable ORR catalytic activity with a half-wave potential at 0.88 V, following a four-electron transfer pathway. Additionally, the introduced cyanurate−glucose composite contributes to the uniform dispersion of Co nanoparticles with an encapsulated carbon layer in Co-N/C-800@MCA-ZIF-67-C, thereby providing remarkable electrochemical stability, as evidenced by only a 9.7% decay after 98,000 s and excellent methanol tolerance. Furthermore, a peak power density of 178 mW cm^{-2} and a long lifetime durability of 150 h at 10 mA cm^{-2} were achieved in the liquid zinc−air battery.

■ ASSOCIATED CONTENT

ⓈⅠ Supporting Information

The Supporting Information is available free of charge at https://pubs.acs.org/doi/10.1021/acsomega.3c07229.

> SEM images, TEM images, XPS full spectrum analysis, split-peak fit, elemental contents for the catalysts derived from different samples and heating temperatures, XRD patterns, raman spectra, N2 adsorption-desorption isotherms, pore size distribution diagram, LSV polarization curves, CV curves, methanol tolerance test, LSV polarization curves, Raman and XPS characterizations, characterizations of N2 adsorption-desorption, and performance comparison (PDF)

■ AUTHOR INFORMATION

Corresponding Authors

Yapeng Cheng − *State Key Laboratory of Advanced Technology for Materials Synthesis and Processing, Wuhan University of Technology, Wuhan 430070, China;* ⓞ orcid.org/0000-0002-9218-9095; Email: 266011@ whut.edu.cn

Jin Liu − *State Key Laboratory of Advanced Technology for Materials Synthesis and Processing, Wuhan University of Technology, Wuhan 430070, China; School of Chemistry and Material Science, Hubei Engineering University, Xiaogan 432000, People's Republic of China;* Email: liu.j@ hbeu.edu.cn

Authors

Peipei Liu − *State Key Laboratory of Advanced Technology for Materials Synthesis and Processing, Wuhan University of Technology, Wuhan 430070, China; Foshan Xianhu*

Laboratory of the Advanced Energy Science and Technology Guangdong Laboratory, Foshan 528200, China

Meiling Fan − *State Key Laboratory of Advanced Technology for Materials Synthesis and Processing, Wuhan University of Technology, Wuhan 430070, China; Xiangyang Polytechnic, Xiangyang 441050, China*

Hongfei Pan − *State Key Laboratory of Advanced Technology for Materials Synthesis and Processing, Wuhan University of Technology, Wuhan 430070, China; Foshan Xianhu Laboratory of the Advanced Energy Science and Technology Guangdong Laboratory, Foshan 528200, China;* orcid.org/0000-0002-6472-226X

Haining Zhang − *State Key Laboratory of Advanced Technology for Materials Synthesis and Processing, Wuhan University of Technology, Wuhan 430070, China; Foshan Xianhu Laboratory of the Advanced Energy Science and Technology Guangdong Laboratory, Foshan 528200, China; Hubei Key Laboratory of Fuel Cell Technology, Wuhan University of Technology, Wuhan 430070, China;* orcid.org/0000-0002-5546-2347

Complete contact information is available at:
https://pubs.acs.org/10.1021/acsomega.3c07229

Author Contributions

#P.L. and M.F. contributed to the work equally and should be regarded as cofirst authors.

Notes

The authors declare no competing financial interest.

■ REFERENCES

(1) Zhang, D.; Li, Y.; Li, Y.; Zhan, S. Towards single-atom photocatalysts for future carbon-neutral application. *Smart Mater.* **2022**, *3*, 417−446.

(2) Li, P.; Li, J.; Cui, L.; Zhang, Y.; Fan, K.; Li, B.; Zong, L.; Wang, L. Boosting the oxygen reduction reaction behaviour of Ru single atoms in porous carbon nanospheres via microscopic coordination environment manipulation. *Appl. Surf. Sci.* **2023**, *615*, 156304.

(3) Liu, Q.; Chang, Z.; Li, Z.; Zhang, X. Flexible Metal-Air Batteries: Progress, Challenges, and Perspectives. *Small Methods* **2018**, *2*, 1700231.

(4) Zhang, H.; Huang, S.; Salla, M.; Zhuang, J.; Gao, M.; Lek, D. G.; Ye, H.; Wang, Q. A Redox-Mediated Zinc-Air Fuel Cell. *ACS Energy Lett.* **2022**, *7*, 2565−2575.

(5) Lee, J.-S.; Tai Kim, S.; Cao, R.; Choi, N.-S.; Liu, M.; Lee, K. T.; Cho, J. Metal-Air Batteries with High Energy Density: Li-Air versus Zn-Air. *Adv. Energy Mater.* **2011**, *1*, 34−50.

(6) Liu, M.; Zhao, Z.; Duan, X.; Huang, Y. Nanoscale Structure Design for High-Performance Pt-Based ORR Catalysts. *Adv. Mater.* **2019**, *31*, No. e1802234.

(7) Wang, Y.-J.; Long, W.; Wang, L.; Yuan, R.; Ignaszak, A.; Fang, B.; Wilkinson, D. P. Unlocking the door to highly active ORR catalysts for PEMFC applications: polyhedron-engineered Pt-based nanocrystals. *Energy Environ. Sci.* **2018**, *11*, 258−275.

(8) Chen, J.; Li, H.; Fan, C.; Meng, Q.; Tang, Y.; Qiu, X.; Fu, G.; Ma, T. Dual Single-Atomic Ni-N$_4$ and Fe-N$_4$ Sites Constructing Janus Hollow Graphene for Selective Oxygen Electrocatalysis. *Adv. Mater.* **2020**, *32*, No. e2003134.

(9) Sun, Y.; Sun, S.; Yang, H.; Xi, S.; Gracia, J.; Xu, Z. J. Spin-Related Electron Transfer and Orbital Interactions in Oxygen Electrocatalysis. *Adv. Mater.* **2020**, *32*, No. e2003297.

(10) Khalil, E. M. A.; ElBatal, F. H.; Hamdy, Y. M.; Zidan, H. M.; Aziz, M. S.; Abdelghany, A. M. Infrared absorption spectra of transition metals-doped soda lime silica glasses. *Phys. B* **2010**, *405*, 1294−1300.

(11) Chao, S.; Geng, M. 3,5-Diamino-1,2,4-triazole as a Nitrogen precursor to synthesize highly efficient Co-N/C non-precious metal bifunctional catalyst for oxygen reduction reaction and oxygen evolution reaction. *Int. J. Hydrogen Energy* **2016**, *41*, 12995−13004.

(12) Wang, J.; Li, L.; Chen, X.; Lu, Y.; Yang, W.; Duan, X. A Co-N/C hollow-sphere electrocatalyst derived from a metanilic CoAl layered double hydroxide for the oxygen reduction reaction, and its active sites in various pH media. *Nano Res.* **2017**, *10*, 2508−2518.

(13) Amiinu, I. S.; Liu, X.; Pu, Z.; Li, W.; Li, Q.; Zhang, J.; Tang, H.; Zhang, H.; Mu, S. From 3D ZIF Nanocrystals to Co-N$_x$/C Nanorod Array Electrocatalysts for ORR, OER, and Zn-Air Batteries. *Adv. Funct. Mater.* **2018**, *28*, 1704638.

(14) Li, B. Q.; Zhao, C. X.; Liu, J. N.; Zhang, Q. Electrosynthesis of Hydrogen Peroxide Synergistically Catalyzed by Atomic Co-N$_x$-C Sites and Oxygen Functional Groups in Noble-Metal-Free Electrocatalysts. *Adv. Mater.* **2019**, *31*, 1904044.

(15) Zhu, Y.; Zhang, B.; Liu, X.; Wang, D.-W.; Su, D. S. Unravelling the Structure of Electrocatalytically Active Fe-N Complexes in Carbon for the Oxygen Reduction Reaction. *Angew. Chem., Int. Ed.* **2014**, *53*, 10673−10677.

(16) Wang, D.; Pan, X.; Yang, P.; Li, R.; Xu, H.; Li, Y.; Meng, F.; Zhang, J.; An, M. Transition Metal and Nitrogen Co-Doped Carbon-based Electrocatalysts for the Oxygen Reduction Reaction: From Active Site Insights to the Rational Design of Precursors and Structures. *ChemSusChem* **2021**, *14*, 33−55.

(17) Wan, X.; Liu, X.; Li, Y.; Yu, R.; Zheng, L.; Yan, W.; Wang, H.; Xu, M.; Shui, J. Fe-N-C electrocatalyst with dense active sites and efficient mass transport for high-performance proton exchange membrane fuel cells. *Nat. Catal.* **2019**, *2*, 259−268.

(18) Chen, M. X.; Zhu, M.; Zuo, M.; Chu, S. Q.; Zhang, J.; Wu, Y.; Liang, H. W.; Feng, X. Identification of Catalytic Sites for Oxygen Reduction in Metal/Nitrogen-Doped Carbons with Encapsulated Metal Nanoparticles. *Angew. Chem., Int. Ed.* **2019**, *59*, 1627−1633.

(19) Wang, X.; Fan, X.; Lin, H.; Fu, H.; Wang, T.; Zheng, J.; Li, X. An efficient Co-N-C oxygen reduction catalyst with highly dispersed Co sites derived from a ZnCo bimetallic zeolitic imidazolate framework. *RSC Adv.* **2016**, *6*, 37965−37973.

(20) Mou, J.; Li, Y.; Liu, T.; Zhang, W.; Li, M.; Xu, Y.; Zhong, L.; Pan, W.; Yang, C.; Huang, J.; Liu, M. Metal-Organic Frameworks-Derived Nitrogen-Doped Porous Carbon Nanocubes with Embedded Co Nanoparticles as Efficient Sulfur Immobilizers for Room Temperature Sodium-Sulfur Batteries. *Small Methods* **2021**, *5*, No. e2100455.

(21) Zhang, Y.; Wang, P.; Yang, J.; Lu, S.; Li, K.; Liu, G.; Duan, Y.; Qiu, J. Decorating ZIF-67-derived cobalt-nitrogen doped carbon nanocapsules on 3D carbon frameworks for efficient oxygen reduction and oxygen evolution. *Carbon* **2021**, *177*, 344−356.

(22) Wang, J.; Liang, J.; Liu, P.; Yan, Z.; Cui, L.; Yue, L.; Zhang, L.; Ren, Y.; Li, T.; Luo, Y.; Liu, Q.; Zhao, X.-E.; Li, N.; Tang, B.; Liu, Y.; Gao, S.; Asiri, A. M.; Hao, H.; Gao, R.; Sun, X. Biomass Juncus derived carbon decorated with cobalt nanoparticles enables high-efficiency ammonia electrosynthesis by nitrite reduction. *J. Mater. Chem. A* **2022**, *10*, 2842−2848.

(23) Wang, L.; Li, Z.; Du, C.; Han, Y.; Yang, J. High-temperature graphitization of coke and lithium storage properties of coke-based graphite. *Int. J. Coal Prep. Util.* **2023**, 1−18.

(24) Yang, J.; Yu, C.; Fan, X.; Liang, S.; Li, S.; Huang, H.; Ling, Z.; Hao, C.; Qiu, J. Electroactive edge site-enriched nickel-cobalt sulfide into graphene frameworks for high-performance asymmetric super-capacitors. *Energy Environ. Sci.* **2016**, *9*, 1299−1307.

(25) Peng, Y.; Zhang, F.; Zhang, Y.; Luo, X.; Chen, L.; Shi, Y. ZnS modified N, S dual-doped interconnected porous carbon derived from

dye sludge waste as high-efficient ORR/OER catalyst for rechargeable zinc-air battery. *J. Colloid Interface Sci.* **2022**, *616*, 659−667.

(26) Zhong, K.; Lu, X.; Dai, Y.; Yang, S.; Li, J.; Zhang, H.; Wang, Y.; Zuo, J.; Tang, J.; Su, M. UiO66-NH₂ as self-sacrificing template for Fe/N-doped hierarchically porous carbon with high electrochemical performance for oxygen reduction in microbial fuel cells. *Electrochim. Acta* **2019**, *323*, 134777.

(27) Kim, K.; Kim, Y.; Kim, J. Enhanced cathodic catalytic activity of an N-doped micropore structure obtained through the six-coordinate bond of an EDTA-Ce composite for the oxygen reduction reaction. *Appl. Surf. Sci.* **2020**, *505*, 144418.

(28) Chen, T.; Ma, J.; Chen, S.; Wei, Y.; Deng, C.; Chen, J.; Hu, J.; Ding, W. Construction of heterostructured CoP/CN/Ni: Electron redistribution towards effective hydrogen generation and oxygen reduction. *Chem. Eng. J.* **2021**, *415*, 129031.

(29) Pan, Q.-R.; Lai, B.-L.; Huang, L.-J.; Feng, Y.-N.; Li, N.; Liu, Z.-Q. Regulating the Electronic Structure of Cu-N$_x$ Active Sites for Efficient and Durable Oxygen Reduction Catalysis to Improve Microbial Fuel Cell Performance. *ACS Appl. Mater. Interfaces* **2023**, *15*, 1234−1246.

(30) Pimperl, N.; Bevilacqua, N.; Schmid, M. A.; Loichet Torres, P. A.; El-Sayed, H. A.; Zeis, R.; Zeyer, K. P. Nitrogen-functionalized carbon-supported Pt catalysts implemented in high-temperature polymer electrolyte membrane fuel cell. *J. Power Sources* **2021**, *507*, 229971.

(31) Shen, T.; Huang, X.; Xi, S.; Li, W.; Sun, S.; Hou, Y. The ORR electron transfer kinetics control via Co-N and graphitic N sites in cobalt single atom catalysts in alkaline and acidic media. *J. Energy Chem.* **2022**, *68*, 184−194.

(32) Kari, J.; Olsen, J. P.; Jensen, K.; Badino, S. F.; Krogh, K. B. R. M.; Borch, K.; Westh, P. Sabatier Principle for Interfacial (Heterogeneous) Enzyme Catalysis. *ACS Catal.* **2018**, *8*, 11966−11972.

(33) Zhang, X.; Xu, J.; Wu, L. Hexamethylenetetramine-derived pyridinic N abundant porous carbon-supported Co/Co-N$_x$ nanoparticles as highly efficient oxygen reduction catalyst and zinc-air battery cathode. *Mater. Today Sustain.* **2022**, *19*, 100180.

(34) Yaengthip, P.; Siyasukh, A.; Payattikul, L.; Kiatsiriroat, T.; Punyawudho, K. The ORR activity of nitrogen doped-reduced graphene oxide below decomposition temperature cooperated with cobalt prepared by strong electrostatic adsorption technique. *J. Electroanal. Chem.* **2022**, *915*, 116366.

(35) Du, C. F.; Song, Q.; Liang, Q.; Zhao, X.; Wang, J.; Zhi, R.; Wang, Y.; Yu, H. The Passive Effect of MXene on Electrocatalysis: A Case of Ti$_3$C$_2$T$_x$/CoNi-MOF nanosheets for Oxygen Evolution Reaction. *Chem. Nanomater.* **2021**, *7*, 539−544.

(36) Zhang, X.; Lu, P.; Zhang, C.; Cui, X.; Xu, Y.; Qu, H.; Shi, J. Towards understanding ORR activity and electron-transfer pathway of M-N /C electro-catalyst in acidic media. *J. Catal.* **2017**, *356*, 229−236.

(37) Dong, F.; Liu, C.; Wu, M.; Guo, J.; Li, K.; Qiao, J. Hierarchical Porous Carbon Derived from Coal Tar Pitch Containing Discrete Co-N$_x$-C Active Sites for Efficient Oxygen Electrocatalysis and Rechargeable Zn-Air Batteries. *ACS Sustain. Chem. Eng.* **2019**, *7*, 8587−8596.

(38) Ali Khan, A.; Tahir, M. Constructing S-Scheme Heterojunction of CoAlLa-LDH/g-C$_3$N$_4$ through Monolayer Ti$_3$C$_2$-MXene to Promote Photocatalytic CO$_2$ Re-forming of Methane to Solar Fuels. *ACS Appl. Energy Mater.* **2022**, *5*, 784−806.

(39) Liu, Z.; Ye, D.; Zhu, X.; Wang, S.; Zou, Y.; Lan, L.; Chen, R.; Yang, Y.; Liao, Q. ZIF-67-derived Co nanoparticles embedded in N-doped porous carbon composite interconnected by MWCNTs as highly efficient ORR electrocatalysts for a flexible direct formate fuel cell. *Chem. Eng. J.* **2022**, *432*, 134192.

(40) Chen, M.; Fang, H.; Wang, C.; Xu, J.; Wang, L. Enhanced photocatalytic Cr(VI) reduction and H$_2$ production of CdSe quantum dots supported on Co-encapsulated N-doped carbon. *J. Taiwan Inst. Chem. Eng.* **2023**, *146*, 104798.

(41) Hu, Z.; Zhang, Z.; Li, Z.; Dou, M.; Wang, F. One-Step Conversion from Core-Shell Metal-Organic Framework Materials to Cobalt and Nitrogen Codoped Carbon Nanopolyhedra with Hierarchically Porous Structure for Highly Efficient Oxygen Reduction. *ACS Appl. Mater. Interfaces* **2017**, *9*, 16109−16116.

(42) He, T.; Xiong, S.; Han, H.; Wang, D.; Wang, Y.; Dai, C.; Liu, W. Facile synthesis of Ag/GO SERS composite with highly sensitive and stable performance. *Colloids Surf., A* **2023**, *662*, 131008.

(43) Lu, C.; Zhang, J.; Chen, Z.; Jiang, K.; Li, M.; Zhang, F.; Tong, G.; Zou, X.; Su, Y.; Zhuang, X. A room-temperature interfacial approach towards iron/nitrogen co-doped fibrous porous carbons as electrocatalysts for the oxygen reduction reaction and Zn-Air batteries. *Nanoscale* **2019**, *11*, 10257−10265.

(44) Wang, Q.; Gu, Y.; Zhu, W.; Han, L.; Pan, F.; Song, C. Noble-Metal-Assisted Fast Interfacial Oxygen Migration with Topotactic Phase Transition in Perovskite Oxides. *Adv. Funct. Mater.* **2021**, *31*, 2106765.

(45) Chang, S.; Zhang, H.; Zhang, Z. FeCo alloy/N, S dual-doped carbon composite as a high-performance bifunctional catalyst in an advanced rechargeable zinc-air battery. *J. Energy Chem.* **2021**, *56*, 64−71.

(46) Li, L.; Wen, Y.; Han, G.; Kong, F.; Du, L.; Ma, Y.; Zuo, P.; Du, C.; Yin, G. Architecting FeN$_x$ on High Graphitization Carbon for High-Performance Oxygen Reduction by Regulating d-Band Center. *Small* **2023**, *19*, 2300758.

(47) Tang, J.; Salunkhe, R. R.; Zhang, H.; Malgras, V.; Ahamad, T.; Alshehri, S. M.; Kobayashi, N.; Tominaka, S.; Ide, Y.; Kim, J. H.; Yamauchi, Y. Bimetallic Metal-Organic Frameworks for Controlled Catalytic Graphitization of Nanoporous Carbons. *Sci. Rep.* **2016**, *6*, 30295.

(48) Li, Y.; Liao, W.; Li, Z.; Feng, T.; Sun, L.; Guo, C.; Zhang, J.; Li, J. Building three-dimensional porous nano-network for the improvement of iron and nitrogen-doped carbon oxygen reduction electrocatalyst. *Carbon* **2017**, *125*, 640−648.

(49) Wu, H.; Li, H.; Zhao, X.; Liu, Q.; Wang, J.; Xiao, J.; Xie, S.; Si, R.; Yang, F.; Miao, S.; Guo, X.; Wang, G.; Bao, X. Highly doped and exposed Cu(i)-N active sites within graphene towards efficient oxygen reduction for zinc-air batteries. *Energy Environ. Sci.* **2016**, *9*, 3736−3745.

(50) Shao, C.; Liao, F.; Zhu, W.; Zhang, Y.; Ma, M.; Yang, J.; Yin, K.; Shao, M.; Jiang, B. Carbon dots bridge NiO and Mn$_2$O$_3$ as highly efficient bifunctional oxygen electrocatalysts for rechargeable zinc-air batteries. *Appl. Surf. Sci.* **2022**, *596*, 153642.

(51) Tao, J.; Wang, X.; Xu, M.; Liu, C.; Ge, J.; Xing, W. Non-noble metals as activity sites for ORR catalysts in proton exchange membrane fuel cells (PEMFCs). *Ind. Chem. Mater.* **2023**, *1*, 388−409.

(52) Xie, X.; Shang, L.; Shi, R.; Waterhouse, G. I. N.; Zhao, J.; Zhang, T. Tubular assemblies of N-doped carbon nanotubes loaded with NiFe alloy nanoparticles as efficient bifunctional catalysts for rechargeable zinc-air batteries. *Nanoscale* **2020**, *12*, 13129−13136.

(53) Wang, Q.; Shang, L.; Shi, R.; Zhang, X.; Zhao, Y.; Waterhouse, G. I. N.; Wu, L.-Z.; Tung, C.-H.; Zhang, T. NiFe Layered Double Hydroxide Nanoparticles on Co, N-Codoped Carbon Nanoframes as Efficient Bifunctional Catalysts for Rechargeable Zinc-Air Batteries. *Adv. Energy Mater.* **2017**, *7*, 1700467.

(54) Wang, M.; Wang, H.; Ren, J.; Wang, X.; Wang, R. FeCo nanoclusters inserted N,S -doped carbon foams as bifunctional electrocatalyst for high-performance rechargeable Zn-air batteries. *J. Power Sources* **2022**, *538*, 231592.

(55) George, T. Y.; Asset, T.; Avid, A.; Atanassov, P.; Zenyuk, I. V. Kinetic Isotope Effect as a Tool To Investigate the Oxygen Reduction Reaction on Pt-based Electrocatalysts-Part I: High-loading Pt/C and Pt Extended Surface. *ChemPhysChem* **2020**, *21*, 469−475.

(56) Liu, C.; Miao, C.; He, M.; Wang, J.; Chen, Q.; Nie, S.; Xiao, W. Optimized layered ternary LiNi$_{0.5}$Co$_{0.2}$Mn$_{0.3}$O$_2$ cathode materials modified with ultrathin Li$_3$InCl$_6$ fast ion conductor layer for lithium-ion batteries. *J. Power Sources* **2023**, *566*, 232961.

(57) Xin, Y.; Pan, S.; Hu, X.; Miao, C.; Nie, S.; Mou, H.; Xiao, W. Engineering amorphous SnO2 nanoparticles integrated into porous

N-doped carbon matrix as high-performance anode for lithium-ion batteries. *J. Colloid Interface Sci.* **2023**, *639*, 133−144.

(58) Wang, J.; Yi, Z.; Liu, C.; He, M.; Miao, C.; Li, J.; Xu, G.; Xiao, W. Revealing the effect of Nb^{5+} on the electrochemical performance of nickel-rich layered $LiNi_{0.83}Co_{0.11}Mn_{0.06}O_2$ oxide cathode for lithium-ion batteries. *J. Colloid Interface Sci.* **2023**, *635*, 295−304.

(59) Wang, J.; Liu, C.; Xu, G.; Miao, C.; Wen, M.; Xu, M.; Wang, C.; Xiao, W. Strengthened the structural stability of in-situ F^- doping Ni-rich $LiNi_{0.8}Co_{0.15}Al_{0.05}O_2$ cathode materials for lithium-ion batteries. *Chem. Eng. J.* **2022**, *438*, 135537.